Case History

Moisture estimation within a mine heap: An application of cokriging with assay data and electrical resistivity

Dale Rucker[1]

ABSTRACT

Cokriging has been applied to estimate the distribution of moisture within a rock pile of low-grade gold ore, or heap. Along with the primary data set of gravimetric moisture content obtained from drilling, electrical resistivity was used to supplement the estimation procedure by supplying a secondary data set. The effectiveness of the cokriging method was determined by comparing the results to kriging the moisture data alone and through least-squares regression (LSR) modeling of colocated resistivity and moisture. In general, the wells from which moisture data were derived were separated by distances far greater than the horizontal correlation scale. The kriging results showed that regions generally undersampled by drilling reverted to the mean of the moisture data. The LSR technique, which provides a simple transformation of resistivity to moisture, converted the low resistivity to highmoisture, and vice versa. The sparse well locations created a high degree of uncertainty in the transformed data set. Extreme resistivity values produced nonphysical moisture values, either negative for the linear model or values greater than one for the power model. The cokriging application, which considers the correlation scale and secondary data, produced the best results, as indicated through the cross validation. The mean and variance of the cokriged moisture were closer to the measured moisture, and the bias in the residuals was the lowest. The application likely could be improved through optimal well placement, whereby the resistivity results guide the drilling program through gross target characterization, and the moisture estimation could be updated iteratively.

INTRODUCTION

Modern mining relies on the heap leaching process to extract metal from rock (e.g., Burkin, 2001; Han, 2002). Heap leaching is a method of applying a dilute aqueous ionic solution to the surface of a pile of prepared ore (Juvonen and Kontas, 1999). Ore preparation can include crushing, agglomeration, or run-of-mine (ROM), depending on the geology and amount of fine-grained material. The leachate is allowed to percolate through the pile to solubilize and mobilize the metal (Crundwell and Godorr, 1997; De Andrade Lima and Hodouin, 2005; Bouffard and Dixon, 2007), and the leaching solution is either acidic or basic, depending on the metal. A basic sodium cyanide solution, for example, is used to extract gold by forming aurocyanide (Habashi, 1966; Marsden and House, 1992). Gold extraction can be enhanced also by pretreatment with biological agents or through roasting (Iglesias and Carranza, 1994). Beneath the heap,

a liner and drainage pipe network collects the pregnant leach solution (PLS) for final processing, including solvent extraction and electrowinning.

The application rate of leaching solution to the surface of a heap is approximately 5 to 15 L/h per square meter of surface area, and effective leaching of the ore is impacted greatly by the types of geologic materials used in the construction, how they were placed, and the degree of fines. In general, heaps are large heterogeneous rock piles of differing geologic media taken from various parts of an open pit (see Kennedy, 1990). The heap at the Round Mountain Mine in central Nevada, for example, spans approximately 1600 m by 800 m and is more than 150 m tall, with gold occurring in tuff, limestone, and quaternary alluvium (Mills, 1985). These different types of deposits have their own grain-size distribution and controlling factors for lixiviant flow.

Ineffective leaching within the heap typically is the result of factors that can include the tendency of finer-grained material to compact into confining zones, wetting front instability, and channeling along "fractures" of well-sorted, coarse-grained material (Kunkel and Arnold, 2008). The creation of confining zones, for example, causes pooling and shading. The pooling of lixiviant occurs when solution accumulates above the confining zone, where the hydraulic conductivity of the zone is sufficiently low that percolation through the zone occurs at very large time scales. The pooling then causes additional water to cascade around the confining zone and create a shading effect immediately below. The shaded region remains relatively dry, reducing the total volume of leached ore. Large confining zones therefore reduce the total effectiveness of the heap and leave large metal inventories in place.

Targeting the dry zones with a secondary leaching application, such as Hydro-Jex (Seal, 2004, 2007), increases the yield and efficiency of a heap. The secondary leaching process consists of drilling and casing holes within a heap, perforating the casing at specific depth intervals, and injecting leachate at high pressures within each depth interval using a straddle packer. The challenge then becomes the characterization of the heap and effective well siting. Given the cost of well drilling and assaying, indiscriminate well placement could absorb the additional profit gained through secondary recovery.

Heap characterization can be conducted through direct and indirect means. Direct characterization includes hard information obtained from assay results during drilling. Indirect characterization can include inexpensive geophysical surveys, and the mining industry has relied traditionally on geophysics, primarily for the initial exploration of mineral resources. Geophysics, however, can be applied to near-surface problems to understand more fully the distribution of resources and moisture in an engineered earth. Examples of geophysics applied to engineered structures include levees (Asch et al., 2008), dams (Osazuwa and Chinedu, 2008), and foundations (Dong et al., 2008). The geophysical data usually are considered soft, as unique relationships between the geophysical property and the desired heap property (water content, gold concentration, and so on) are rare. Many competing factors can give rise to similar values of the measured geophysical property, and it is necessary to combine the hard and soft data to form a complete conceptual model of the subsurface.

In this study, we present a method of combining hard assay data and soft geophysical data for characterizing an active heap using geostatistics. The assay data include gravimetric water content (mass-based moisture content as defined in Topp and Ferré, 2002), and the geophysical data include electrical resistivity, acquired along transects on the surface of the heap and inverse modeled using a 3D resistivity code. This study follows an approach similar to Parks and Bentley (1996), whereby several geostatistical methods are tested and compared, including kriging of the assay data alone, least-squares regression (LSR) of the assay and resistivity data, and cokriging of the assay and resistivity data. Although geophysical characterization of waste rock piles is shown in the literature (e.g., Campos et al., 2003; Gloaguen et al., 2007; Poisson et al., 2009), this study explores an active heap to help increase gold production by providing the means for better well siting for secondary recovery methods.

SITE DESCRIPTION

Figure 1 shows the site location of the North Area Leach (NAL) pad at Newmont Mining Corporation's Carlin, Nevada, operations. The mine is 20 miles north of Carlin, Nevada, U.S.A. The NAL pad was constructed in 1987 to process low-grade oxide gold ores mined from multiple open pits on the Carlin Trend. It was constructed as a fully lined facility in a series of phased expansions.

The heap under investigation was underlaid with synthetic liners placed directly on a prepared native soil base. An underdrain solution collection system, composed of four-inch perforated polyvinyl chloride (PVC) pipe, lies on top of the synthetic liner. The ore consisted of ROM and crushed rock. Since 2004, however, only ROM ore has been placed. Lime is added directly to the ore and to the lixiviant to increase the pH for effective gold removal. The ore is placed by end dumping from 250-ton trucks in nominal 10-meter lifts with an ultimate heap height of 100 meters.

Gold is leached from the ore with a dilute sodium cyanide solution, which is applied to the surface of the heap using drip emitters. Typical solution application rates of 12.2 L/h/m^2 are used with a primary leach cycle lasting 90 to 120 days. Total barren solution flows from the heap at a rate of approximately 1.82×10^6 L/h. Gold is recovered from the pregnant solution by means of a carbon-in-column (CIC) plant. As of December 2008, more than 208 million tons have been placed, from which three million ounces of gold have been recovered. The heap construction and leaching process is similar to that of pads on adjacent properties (see Bhakta and Arthur, 2002).

It is suspected that a significant quantity of gold remains in the heap, prompting Newmont to consider secondary recovery using
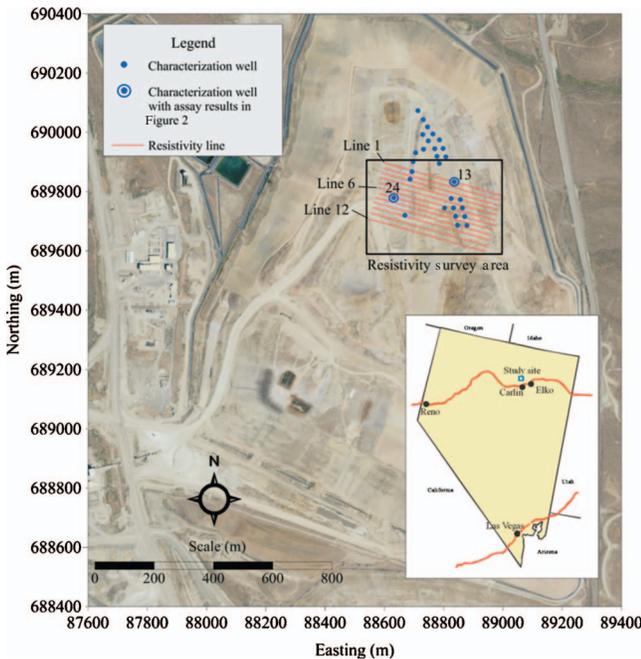
Figure 1. Site location of the North Area Leach (NAL) pad, north of Carlin, Nevada, U.S.A. Coordinates are in Nevada State Plane, meters, North American datum of 1927.

pressurized injections (Rucker et al., 2009b). The injections are used to push lixiviant into unleached or minimally leached zones through perforated wells. To site the wells better for secondary recovery, drilling and assaying along with electrical resistivity imaging were conducted on the pad. Twenty-nine wells were placed as low as a depth of 60 m below the pad surface (BPS), and samples were extracted and characterized every 1.5 m for gravimetric moisture content, gold, pH, and other information.

A total of 983 samples were used to characterize the pad with hard data. The moisture content ranged from very dry (0.005 g/g) to moist (0.28 g/g). The aurocyanide concentration ranged from 1×10^{-4} ounces per ton of ore (OPT) to 6.21×10^{-2} OPT. Economically, aurocyanide concentrations greater than 6×10^{-3} OPT are of interest at NAL, which accounted for 186 samples. The pH generally was between 7 and 10 with a few values falling below 7 and a few near 11. The average pH was 8.15. Figure 2 shows the assay data for wells 13 and 24 at NAL. The data appear rather heterogeneous, with moisture in particular changing dramatically over very short distances.

For this work, we chose the geostatistical method of ordinary kriging to estimate the distribution of moisture in the heap. Kriging uses a weighted linear combination of neighboring values to estimate the value at the unsampled location. The following section describes the theory and results of kriging moisture data over the heap.

We are at an advantage, however, because we also have a 3D representation of electrical resistivity over a portion of the pad, which can be used for cokriging the hard and soft data together, assuming that the two data sets have some spatial correlation. Figure 1 shows the outline of the resistivity area in the center of the pad. Cokriging is similar to kriging, whereby a weighted linear combination of hard

and soft data is used to calculate the value at the unsampled location. The cokriging method also can accommodate either type of data that do not necessarily coexist at the same location, allowing for the highly resolved resistivity to be incorporated with low-resolution assays.

THEORY

Geostatistics

Geostatistics offers a way of describing the spatial continuity of natural phenomena and providing a means of interpolation (or extrapolation) at an unsampled location u_0 (Isaaks and Srivastava, 1989). For the kriging and cokriging methods, the variogram or covariance functions are used to estimate the spatial continuity of the sample population. These functions aim to measure the average degree of dissimilarity between an unsampled value $\mathbf{z}(u)$ and a nearby data value $\mathbf{z}(u + h)$ (Deutsch and Journel, 1992), where h is the lag between the two data points. Typically, larger lags equate to greater dissimilarity between data values.

The covariance is defined for a set of paired data at a given lag as

$$
\begin{aligned}
&\mathrm{Cov}(z(u), z(u + h)) \\
&= C^{zz}(h) \\
&= \left(\frac{1}{n}\right) \sum_{i=1}^{n} (z(u)_i - \bar{z}(u))(z(u + h)_i - \bar{z}(u + h)), \quad (1)
\end{aligned}
$$

where n is the total number of data pairs and the bar notation refers to the mean. In general, the covariance relates how each data value differs from its mean, and a large positive covariance value equates to the paired data responding similarly to their mean (both increasing
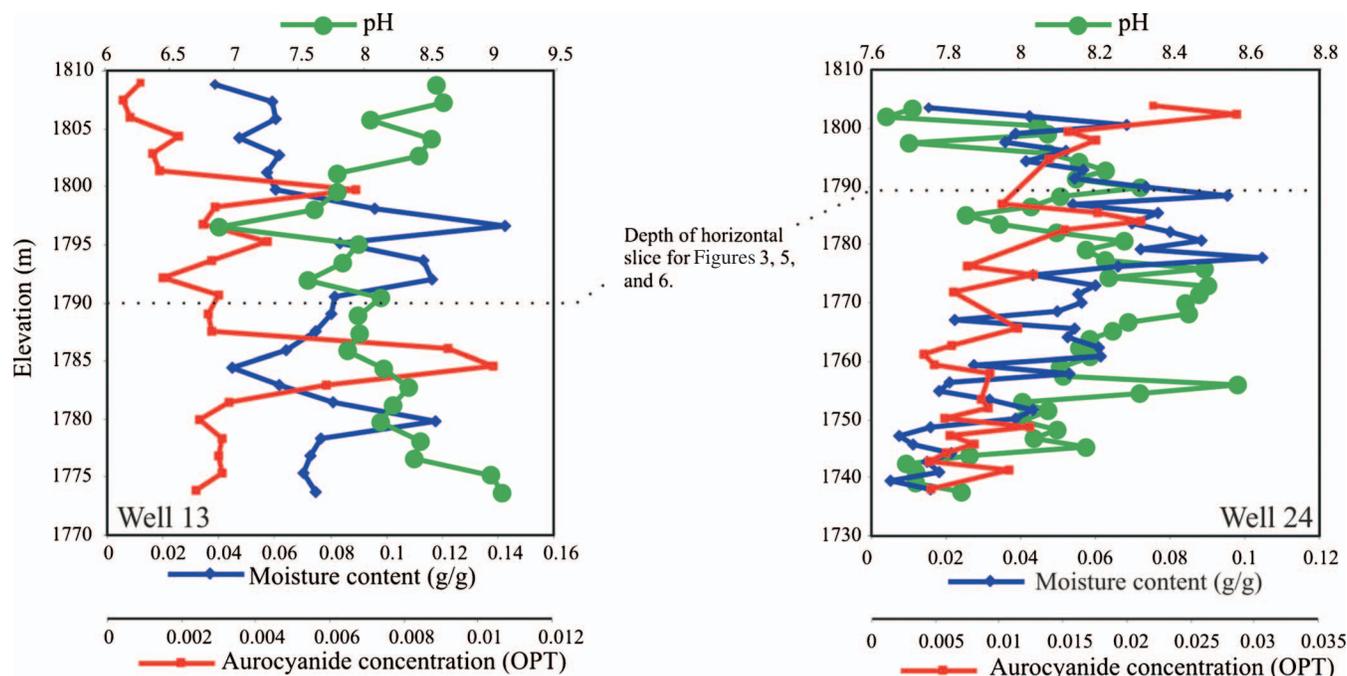
Figure 2. Example data distribution of moisture, leachable gold (as aurocyanide), and pH within two wells, 13 and 24. A moisture content of 0.005 is dry, whereas 0.28 is moist ore.

or decreasing at the same rate). The covariance at $h = 0$ is the variance.

Equation 1 can be applied at many different lags to produce an experimental covariance function, which commonly is plotted as $C^{zz}(0) - C^{zz}(h)$. The experimental covariance function can be represented by a mathematical covariance model, and for this work we primarily used the spherical model,

$$
\begin{aligned}
&C^{zz}(0) - C^{zz}(h) \\
&= \begin{cases} (c_1^z - c_0^z)\left[\dfrac{3h}{2a^z} - \dfrac{1}{2}\left(\dfrac{h}{a^z}\right)^3\right] + c_0^z, & \text{if } h < a \\ c_0^z + c_1^z & \text{if } h \geq a \end{cases},
\end{aligned}
\tag{2}
$$

where c_0^z is the nugget for the covariance model of z, c_1^z is the sill, and a^z is the range. The nugget describes the discontinuity at the origin of the covariance function resulting from short scale variability. The sill is the plateau of the covariance function, and the range is the distance to which the covariance function reaches the sill. The spherical model in general is the most popular model (Isaaks and Srivastava, 1989), but it was chosen here because of its linear behavior near the origin.

The ordinary kriging method uses the covariance model to formulate the weights used in the estimation procedure. The unknown sample z_0 is calculated by

$$
z_0 = \sum_{i=1}^{n} w_i z_i,
\tag{3}
$$

where **w** represents the vector of weights for all known samples. The weights are calculated so that

$$
\sum_{i=1}^{n} w_i = 1,
\tag{4}
$$

to ensure an unbiased estimator. The covariance model of equation 2 then is used with equation 4 to formulate a set of linear equations of the form (Isaaks and Srivastava, 1989)

$$
\sum_{j=1}^{n} w_j C_{ij} + \mu = C_{i0} \quad \forall i = 1 \ldots n
$$

$$
\text{or} \begin{bmatrix} C_{11} & \cdots & C_{1n} & 1 \\ \vdots & \ddots & \vdots & \vdots \\ C_{n1} & \cdots & C_{nn} & 1 \\ 1 & \cdots & 1 & 0 \end{bmatrix} \cdot \begin{bmatrix} w_1 \\ \vdots \\ w_n \\ \mu \end{bmatrix} = \begin{bmatrix} C_{10} \\ \vdots \\ C_{n0} \\ 1 \end{bmatrix},
\tag{5}
$$

where C_{ij} is the covariance for data z_i and z_j at a separation of h_{ij} and μ is the Lagrange parameter (Isaaks and Srivastava, 1989). The right-hand side of equation 5 is the covariance between z_i and unsampled z_0.

To demonstrate, the moisture data from all wells at NAL were kriged over the domain encompassing the resistivity measurements. The spherical covariance function was used:

$$
C^{zz}(0) - C^{zz}(h) = c_0^z + \text{Sph}\begin{pmatrix} {_1}a^z \\ {_1}c_1^z \end{pmatrix} + \text{Sph}\begin{pmatrix} {_2}a^z \\ {_2}c_1^z \end{pmatrix}
$$

$$
C^{zz}(0) - C^{zz}(h) = 0.4 \cdot 10^{-3} + \text{Sph}\begin{pmatrix} 40 \\ 0.4 \cdot 10^{-3} \end{pmatrix}
$$

$$
+ \text{Sph}\begin{pmatrix} 100 \\ 0.03 \cdot 10^{-3} \end{pmatrix},
\tag{6}
$$

where Sph indicates the spherical form of the covariance model. Multiple models can be compounded, where, for example, the first spherical covariance model operates in the range ($_1a^z$) of 0 to 40 m, and the second spherical covariance model operates in the range of 40 to 100 m ($_2a^z$); $_1c_1^z$ is the sill for the first range of $_1a^z$, and $_2c_1^z$ is the sill for the second range. Beyond 100 m, the covariance flattens to a value of $c_0^z + {_1}c_1^z + {_2}c_1^z$.

Figure 3 shows the results of the kriging as a slice through the heap at a constant elevation of 1790 m above mean sea level (approximately 15 m BPS). Figure 3a is the covariance function and the model fit to the covariance function as described in equation 6. The experimental covariance function is smoothly varying out to about 40 m, which is the average depth for the wells. Beyond 40 m, the covariance function is quite noisy, and the range and sill for the larger lags were estimated by judgment. The initial 40-m range of the first spherical model coincides with the average length of the wells, suggesting that there is more consistency in the vertical than in the lateral direction.

Figure 3b shows the kriging results for a horizontal slice through the heap at a constant elevation of 1790 m. The MATLAB program COKRI (Marcotte, 1991, 1993) was used to krige the data at 1680 locations on the planar surface (coincident with electrode locations described in geophysical surveying methodology). For the isolated wells in the western and northern regions, the moisture content shows rings around the wells that extend about 40 m. Greater than 40 m, the moisture is roughly the mean of all moisture measurements. For the cluster of wells in the eastern region, greater variability is seen immediately around and between the wells. Away from the well cluster, the moisture returns to a mean value, suggesting that an accurate assay-based characterization of this heap likely would require wells placed every 30 to 40 m.

Cross validation is a means of testing the covariance model and kriging method by serially estimating the unknown value at an already sampled location. The sampled value is removed from the population, and the estimated result is compared to the true value. Figure 3c shows the results of the cross validation by removing a single measurement point for reestimation. The scatter plot shows a relatively good fit considering the heterogeneous nature of the parameter. However, because the point measurements are separated by only 1.5 m along the length of the well, measurements above and below the removed sample strongly influence the outcome. Furthermore, the point-based cross validation says nothing about regions that generally are underrepresented. The methodology presented in Figure 3d helps to overcome this by removing measured values from an entire well. All values within the well then are reestimated, and Table 1 lists the statistics for the outcome of this procedure. Clearly, the modeled moisture from kriging reverts to values near the mean, but the variance of the modeled moisture is quite low. There also is a slight bias in the residuals.

Cokriging

Cokriging is similar to kriging, whereby the weighting of primary and secondary (or hard and soft) data remains a linear process:

$$z_0 = \sum_{i=1}^{n} w_i z_i + \sum_{j=1}^{m} \lambda_j v_j$$

$$\text{and } \sum_{i=1}^{n} w_i + \sum_{j=1}^{m} \lambda_j = 1, \tag{7}$$

where v represents the soft data, m is the total number of soft data available for cokriging, and λ is the weighting factor on the soft data. The weights are formulated through covariance models, and cokrig-
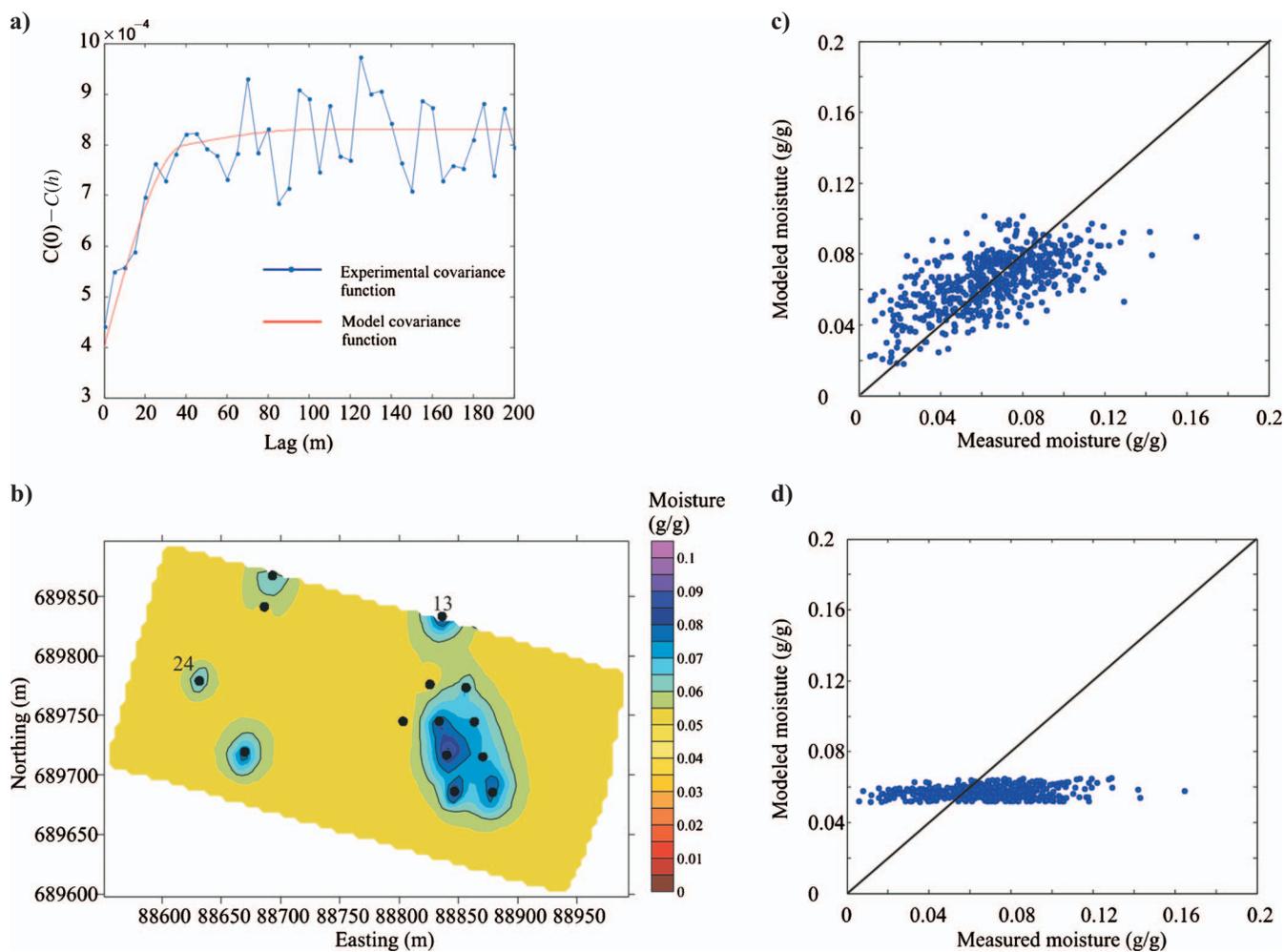
Figure 3. Kriging of moisture data, (a) experimental covariance function and covariance model for moisture, (b) modeled moisture contours at an elevation of 1790 m, (c) cross-validation results from a point-based removal procedure, (d) cross-validation results from a well-based removal procedure. The term lag refers to the distance between data pairs; $C(0) - C(h)$ is the variance minus the covariance of the data pairs separated by a lag of h. Coordinates are in Nevada State Plane, meters, North American datum of 1927.

Table 1. Cross-validated moisture statistics.

Data	Mean	Variance	Mean of residuals	Variance of residuals	rms
Measured	0.068	0.00064			
Kriged (well based)	0.057	0.000011	-0.010	0.00061	0.0266
LSR: Linear fit	0.106	0.0055	0.037	0.0053	1.43
LSR: Power fit	0.089	0.0064	0.022	0.0062	1.58
Cokriged (well based)	0.061	0.000065	-0.0072	0.00063	0.0261

ing with two variables requires three models to be generated: one co-variance model for the primary, one for the secondary, and a cross-covariance model describing the relationship between the primary and secondary variables. The cross-covariance is described by

$$\text{Cov}(z(u),v(u+h)) = C^{zv}(h)$$
$$= \left(\frac{1}{n}\right)\sum_{i=1}^{n}(z(u)_i - \overline{z}(u))(v(u+h)_i$$
$$- \overline{v}(u+h)) \qquad (8)$$

For the cokriging method to be valid and avoid negative variances, the linear model of coregionalization must be used (Ahmed and de Marsily, 1993). The linear model of coregionalization places restrictions on the covariance model (all models must be of the same type), as well as the values for the sill, nugget, and range that can be used in the cross-covariance model,

$$c_0^{zv} \leq (c_0^z c_0^v)$$
$$c_1^{zv} \leq (c_1^z c_1^v),$$
$$a^{zv} \geq (a^z a^v), \qquad (9)$$

where the superscript zv indicates the cross-covariance model parameter, z indicates the primary model parameter, and v indicates the secondary model parameter. One way to help overcome the restrictions of the linear model of coregionalization is to scale the secondary data by the mean of the primary data (Parks and Bentley, 1996). An example of the cokriging method is presented after introducing the electrical resistivity data.

Electrical resistivity

The resistivity method uses electric current (I) that is injected into the earth through one pair of electrodes (transmitting dipole) and measures the resultant voltage potential (V) across another pair of electrodes (receiving dipole). The scalar spatial voltage distribution can be modeled with Poisson's equation (Dey and Morrison, 1979):

$$\frac{\partial}{\partial x}\left(\frac{1}{\rho}\frac{\partial V}{\partial x}\right) + \frac{\partial}{\partial y}\left(\frac{1}{\rho}\frac{\partial V}{\partial y}\right) + \frac{\partial}{\partial z}\left(\frac{1}{\rho}\frac{\partial V}{\partial z}\right) = I \qquad (10)$$

where ρ is the spatially heterogeneous resistivity. The electric current is generated by battery-driven or motor-generator-driven equipment. Field data are acquired using a multielectrode array along lin-

ear transects. A multielectrode array enables rapid data acquisition over a large area with minimal reconfiguration of equipment. Common array configurations include Wenner, Schlumberger, and dipole-dipole arrays.

The Advanced Geosciences Inc. (AGI) system, the SuperSting R8, offers another option, which AGI refers to as the gradient array (AGI, 2008). The gradient array is similar to the Wenner and Schlumberger arrays because the current electrode pair is placed on the two outer electrodes of the basic four-electrode setup, and the voltage is measured on the inner pair. The progression of measurements occurs by moving one current electrode forward along the array and then measuring all adjacent voltage pairs inside the current pair. When the roving current electrode reaches the end of the transect, the other current electrode at the beginning of the line moves forward incrementally and voltage is measured again on all adjacent electrode pairs. The advantages of the gradient array are the large number of measurements and its effective use of the number of available channels on a multichanneled resistivity meter.

Table 2 lists the acquisition statistics for some different array types, with parameters specific to the resistivity meter. For each array comparison, 56 electrodes were used with a measure time of 800 ms using two cycles for repeat error estimation. Acquisition with the gradient array almost doubles the amount of data while using, on average, 7.04 channels (of a total of 8) per reading. The disadvantages of the gradient array are the long acquisition time and the difficulty in conducting a roll along.

After acquisition, the data are preprocessed to remove obvious bad measurements (negative voltages, extremely high voltages, data with high repeat errors, and so on) resulting from random machine error, bad electrode placement, or poor electrode contact with the surrounding material. Unlike the other array types that can be plotted in a logical pseudosection of apparent resistivities, the gradient array does not have an intuitive plotting strategy of apparent resistivity. It is difficult, therefore, to do a preassessment of the spatial arrangement of gradient data prior to inverse modeling. Typically, these data are inverse modeled to find outliers, outliers are removed, and the subset of remaining data is remodeled. The process is repeated until a desired goodness of fit is achieved.

The objective of the inversion is to minimize the difference S between the modeled and measured apparent resistivities, usually in a least-squares sense. The general form of the objective function for the resistivity inversion is based primarily on weighted least squares:

$$\mathbf{S}(m) = (\mathbf{d}_{calc} - \mathbf{d}_{meas})^T \mathbf{W}_d (\mathbf{d}_{calc} - \mathbf{d}_{meas}), \qquad (11)$$

where $\mathbf{d}_{calc}$ is the calculated voltage data from the numerical modeling at coincident locations with $\mathbf{d}_{meas}$, which represents the measured voltage. The expression $\mathbf{W}_d$ represents a weighted function based on the measurement errors and is equal to the inverse of the error covariance matrix. The objective function has been updated many times to include other terms, such as smooth model constraints (i.e., a smooth model based on minimizing the second spatial derivative of the resistivity).

For the inverse models completed on the Newmont Carlin NAL data, the smooth model criterion was invoked, and the final objective function to be minimized for smooth model inversion is represented by

Table 2. Array comparisons for the AGI SuperSting R8 with 56 electrodes, 80-ms time window, and two repeat cycles.

Array	Number of data	Number of command lines	Number of effective channels	Acquisition time (h:mm)
Gradient	2809	399	7.04	0:57
Pole-pole	1540	217	7.1	0:31
Pole-dipole	1485	210	7.07	0:30
Dipole-dipole	1542	272	5.67	0:38
Wenner-Schlumberger	1315	500	2.63	1:11

$$S(m) = (\mathbf{d}_{\text{calc}} - \mathbf{d}_{\text{meas}})^T \mathbf{W}_d (\mathbf{d}_{\text{calc}} - \mathbf{d}_{\text{meas}})$$
$$+ \lambda(\mathbf{m} - \mathbf{m}_0)^T \mathbf{K}(\mathbf{m} - \mathbf{m}_0), \qquad (12)$$

where the second term represents model smoothness, λ is the dampening factor, $\mathbf{m}$ is the model parameter of resistivity at every cell, $\mathbf{m}_0$ is the a priori information and/or initial starting guess, and $\mathbf{K}$ is the difference operator for estimating model smoothness. Changes to the previous model of resistivity distribution $\Delta\mathbf{m}$ occur by

$$[\mathbf{J}^T\mathbf{W}_d\mathbf{J} + \lambda\mathbf{K}]\Delta\mathbf{m} = \mathbf{J}^T\mathbf{W}_d(\mathbf{d}_{\text{calc}} - \mathbf{d}_{\text{meas}}) - \lambda\mathbf{K}(\mathbf{m} - \mathbf{m}_0)$$
$$(13)$$

and

$$\mathbf{m}_{i+1} = \mathbf{m}_i + \Delta\mathbf{m}. \qquad (14)$$

The $(N \times M)\mathbf{J}$ matrix contains the derivative of the simulated data measurements (n) with respect to the model parameters (m) (Gunther et al., 2006).

In general, the automated inversion routine for inverse modeling proceeds as follows:

1. The earth's voltage data have been measured and are discretized into grid nodes using a finite-difference or finite-element mesh. The meshing parameters depend on electrode spacing. The inversion sets out to estimate the true resistivity at every grid node.
2. An initial estimate of the subsurface properties is made based on the literal translation of the pseudosection to a true resistivity, a constant value, or some other distribution from a priori information. The forward model runs with this initial estimate to obtain the distribution of voltages in the subsurface. The root-mean-square (rms) error is calculated between the measured voltage and the calculated voltage.
3. Based on the degree of match between simulated and measured voltages, the initial estimate of resistivity is changed and the forward model is rerun. The iterative method is linearizing a highly nonlinear problem using Newton's method. Essentially, the program solves the linearized problem to obtain the change in modeled resistivity ($\Delta\mathbf{m}$) for the next iteration.
4. The resistivity model is updated using the general formula $\mathbf{m}_{i+1} = \mathbf{m}_i + \Delta\mathbf{m}$, where $\mathbf{m}_{i+1}$ is the resistivity in a model cell at the next iteration, and $\mathbf{m}_i$ is the current value.
5. Steps 3 and 4 are repeated until the rms error changes between successive iterations are less than 10%.

The iterative nature of resistivity inversion is necessary because equation 10 is nonlinear. A more complete discussion of resistivity inversion and the methods by which the true resistivity is calculated can be found in several sources, including Li and Oldenburg (1994), LaBrecque et al. (1996), and Loke and Barker (1996).

GEOPHYSICAL SURVEY METHOD AND RESULTS

The electrical resistivity method was conducted with a multiconductor cable and stainless steel electrodes. The acquisition was conducted one line at a time to create a series of profiles of 2D data. Each line was composed of 140 electrodes, with an electrode spacing of 3 m. Data were acquired using the gradient array for the 12 lines, with a line spacing of 15 m. A total of 1680 electrode locations and

105,840 data values were collected on the heap over a period of six days. After initial noise removal and filtering of substandard data, the net data count was 81,242.

Although the electrical resistivity data were acquired along 2D lines, the data can be combined into a 3D data set given proper georeferencing of the electrodes. For our study, the inversion code EarthImager3DCL (or EI3DCL) by AGI was used to invert the NAL pad resistivity data. The code uses the finite-element numerical method and can incorporate topography. The meshing consisted of tetrahedral elements with 108,976 core nodes (139 rows, 56 columns, 14 layers) on which the electrical resistivity was calculated. For this application, the processing computer system comprised a Dell PowerEdge 6800 running Microsoft Windows Server 2003 64-bit with four dual core Intel Xeon 7120 M processors (3 Ghz) and 32 GB of RAM. To reduce memory requirements, the data were rotated 15.85° counterclockwise, which in effect reduced the number of unique rows and columns in the model domain.

The inverse modeling occurred in two steps. The first step was an initial inversion run with all data after preprocessing. This step required eight iterations to complete in approximately 32.5 hours. The first iteration finished with an rms of 40.55; the last iteration finished with an rms of 20.97. The results of the last iteration then were used for final filtering to remove spurious data that did not fit the overall trend of modeled versus measured voltage. The second step included inverse modeling of a subset of data from the first step, whereby measured voltage data with a difference greater than 20% from the modeled data were removed. The final data count for step two was 65,501. Upon close inspection of the filtered data set used in the inversion, the filtering removed 77 electrodes from the domain likely caused by poor contact and high error, an additional 82 transmitter electrodes (that still were used as receivers), and 37 receiver electrodes (but still used as transmitters). There did not appear to be a pattern or a specific region for the removal of data. The inversion of the reduced data set resulted in the model completing in five iterations to a final rms of 5.77.

Figure 4 shows the 3D distribution of electrical resistivity within the heap. The modeled resistivity values of the heap range from 7.8 to 800 ohm-m, demonstrating that the heap is highly heterogeneous. The inversion model creates a solid block of cells, with each cell having a resistivity value and hence a color associated to it. To provide a means to look within the model, the solid block was sliced horizontally at a depth of 1790 m in Figure 4a. The slice is color contoured with warm colors (red and yellow) representing high resistivity values and cool colors (blue and purple) representing low values. An alternative view of the spatial distribution is to remove all data above (or below) a set resistivity value and show the remaining population as a solid rendered body. Figure 4b shows a solid body of values less than 50 ohm-m, and Figure 4c shows a solid body of values greater than 75 ohm-m. These opaque bodies are presented from overhead and from the south side. Black lines represent the location of electrodes from lines 1 through 12, which are draped over the surface of the heap to give a perspective to the topography.

The distribution of resistivity within the heap shows high values near the surface and in the center of the measurement area. The near surface having high resistivity can be explained through evapotranspiration. High resistivity values can be seen also at breaks in slope on the heap, which are labeled in Figure 4c. It can be reasoned further that the bypassing of leachate along the toe of the heap is caused by a

capillary barrier created by a dipping, fine-grained rock layer overlain on a coarse-grained rock (Rucker et al., 2009a). Low resistivity values, on the other hand, are more common for rock with higher moisture content. The distribution of low resistivity material is observed to be along segregated portions of the measured area and extend as low as the depth of investigation (about 70 m below the heap surface). The depth of investigation is based on the sensitivity of the model cells, and cells below 70 m contributed practically nothing to the inversion procedure. The nature of the resistivity distribution in Figure 4 could suggest preferential flow, whereby gravity drainage along high-permeability zones allows the leachate to shortcut to the drainage system and liner. Most low resistivity regions appear to have a complete connection from top to bottom of the survey area.

MODELING OF ASSAY AND RESISTIVITY DATA

Least-squares regression

Empirical relationships have been developed to describe the observed bulk resistivity of rock cores to water saturation. For sandstones or other high resistivity rock with little to no surface-conduction effects, the Archie relationship can be used:

$$\rho_t = a\rho_w\phi^{-m}S_w^{-n}, \qquad (15)$$

where ρ_t is the resistivity of the rock with fractional saturation, n is the saturation index, ϕ is the porosity, a and m are parameters to de-
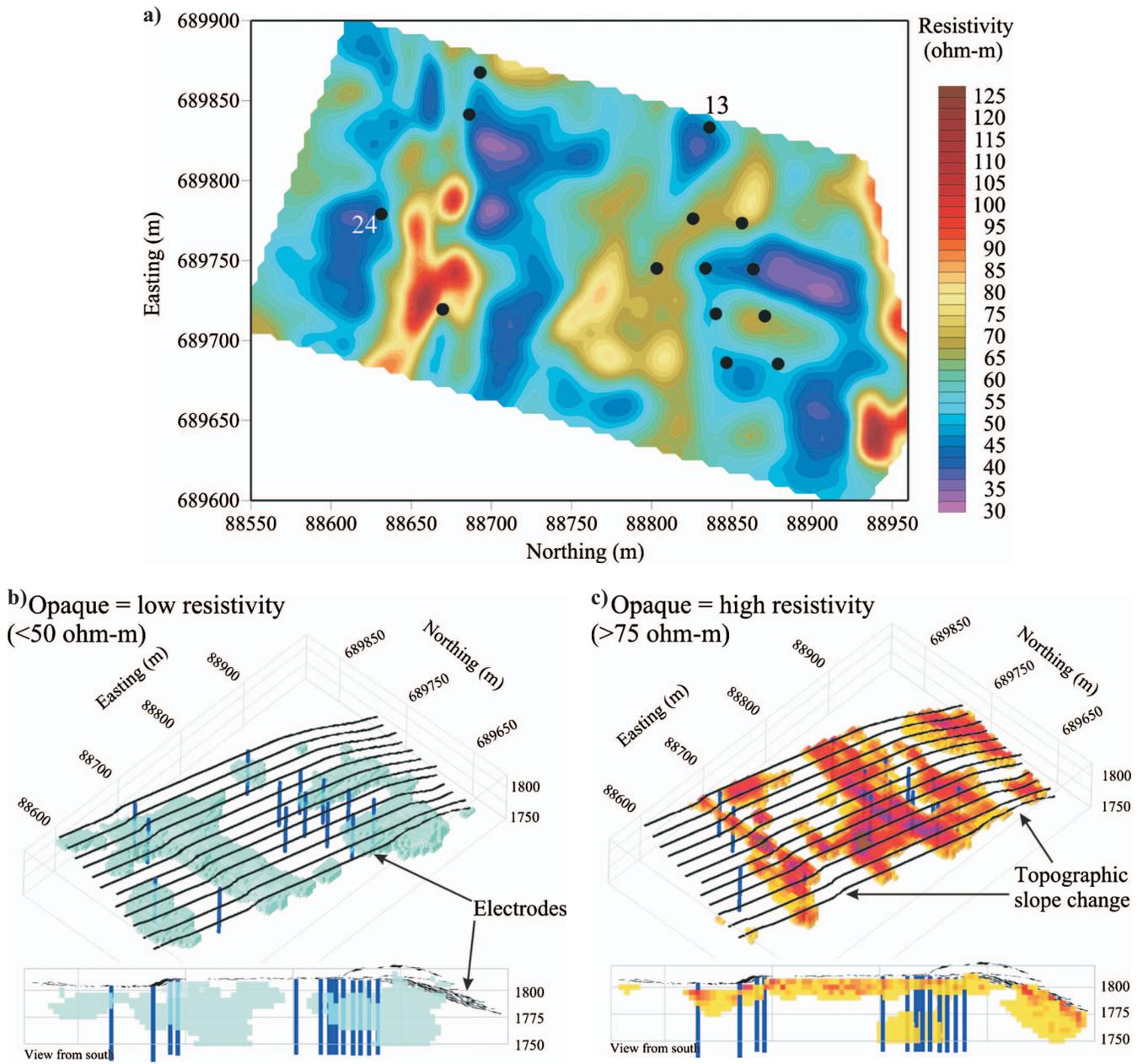
Figure 4. Electrical resistivity distribution within the NAL pad, showing (a) a horizontal slice at an elevation of 1790 m and solid model renderings of (b) low resistivity and (c) high resistivity material. Black lines draped across the surface in (b) and (c) represent electrode locations and give an indication of topography. Coordinates are in Nevada State Plane, meters, North American datum of 1927.

scribe the formation, and ρ_w is the resistivity of the water. Keller (1988) suggests $n = 2$ for sand, and many use this value for their work (see Edwards, 1997; Dannovski and Yaramanci, 1999; Garambois et al., 2002; Descloitres et al., 2008), whereas others observe values less than $n = 2$ (Taylor and Barker, 2006). Grellier et al. (2008) use $n = 2.5$ for a landfill application, and Sen (1997) discusses some reasons for n deviating from its "normal" value of $n = 2$.

Regardless, if $m = n$, then equation 15 can be reduced to

$$\rho_t = a\rho_w\theta_v^{-n} \tag{16}$$

or

$$\rho_t = a\rho_w(D_b\theta_g)^{-n}, \tag{17}$$

where the substitution of $\phi^{-n}S_w^{-n}$ is made for the volumetric water content (θ_v). In equation 17, another substitution of gravimetric water content is made for volumetric water content by incorporating the bulk density (D_b) in g/m³. Guzman et al. (2008) describe several relationships of dry bulk density as a function of heap height, where the bulk density was observed to increase as much as 30% at 80 m BPS.

Other popular petrophysical relationships that account for a conductive matrix include the Waxman Smits (W-S) shaly sandstone model (Waxman and Smits, 1968) and the Hanai-Bruggeman (H-B) effective medium theory (Bussian, 1983), which are presented below (in order) with a partial saturation term:

$$\frac{1}{\rho_t} = \frac{S_w^n}{F}\left(\frac{1}{\rho_w} + \frac{BQ_v}{S_w}\right), \tag{18}$$

$$\rho_t = \rho_w S_w^{-n}\phi^{-m}\left(\frac{1 - \rho_w/\rho_d}{1 - \rho_t/\rho_d}\right)^{-m}, \tag{19}$$

where in the W-S model of equation 18, F is the formation factor, Q_v is the cation exchange capacity per-unit pore volume, and B is the equivalent ionic conductance of clay exchange ions. The remaining term of equation 19 is ρ_d, representing the dispersed-phase resistivity, and Taylor and Barker (2006) describe these equations in more detail.

Although the petrophysical relationships were derived on core samples, whereby all of the parameters that compose the relationships are measured at the same scale, many have adopted them to convert field-based resistivity back to a saturation (or water-content) value. Singha and Gorelick (2006) summarize the complications from this approach, including the mismatch in scale between measurements and the decreased sensitivity of the method away from the electrodes. They conclude that the field-scale relations between electrical resistivity and the hydrogeologic parameter must be site, survey, and inversion specific.

To accommodate these issues, further work summarized in Singha et al. (2007) proposes two new approaches for field-based petrophysics: the full inverse statistical calibration (FISt) and the random field averaging (RFA) methods. Both methods appear to provide a better calibration of the resistivity data by removing the bias typically observed when applying equations 16–19. The FISt method relies on geophysical modeling of hundreds of synthetic realizations of the random distribution of the water content to create petrophysical relationships at every location in space. The realizations and FISt method could be developed for the NAL pad because the basic covariance model has been defined. However, inverse

modeling every realization would be too time-consuming, considering the 32.5 hours necessary to invert a single realization.

The RFA method is less time-consuming and requires only one realization to be inverse modeled. In addition, the RFA method has the same general restrictions necessary for cokriging (Gaussian distribution of both parameters, stationarity, and the same basic covariance model), making the application of RFA to the NAL data set appear doable and preferred. However, the method requires access to internal matrices during the inversion process, namely, the model resolution matrix $\mathbf{R}$ calculated through

$$\mathbf{R} = [\mathbf{J}^T\mathbf{W}_d\mathbf{J} + \alpha\mathbf{K}]^{-1}\mathbf{J}^T\mathbf{W}_d\mathbf{J}. \tag{20}$$

For commercial codes, access to the parameters necessary for calculating $\mathbf{R}$ is either limited or nonexistent. For EI3DCL, there is no access and hence we are stuck with reverting back to fitting relationships to colocated measurements of the hard and soft data regardless of their mismatch in scale. Figure 5a shows the 431 colocated resistivity measurements for moisture and aurocyanide concentration. The high sampling rate of 1.5 m within the borehole meant that several moisture data values fell within a resistivity model cell. For this exercise, each of these data was considered independently; that is, several moisture values were compared to a single resistivity value. Averaging all moisture values that fell within each resistivity block was considered also, but that would have smoothed the moisture data unnecessarily.

Figure 5 shows the results of least-squares regression (LSR) for moisture and resistivity (presented here as electrical conductivity [EC]). Figure 5a is the scatter of colocated EC versus moisture, whereby two regression models have been developed: a linear and a power function. The scatter generally shows a direct relationship between the two data, although weak. The power function model is an obvious choice for a fit to the data, based on the form of equation 17. The linear fit is based on a common methodology in science to relate two variables; it is not based on a physical model. A high degree of scatter appears to exist between the two variables, with a low correlation coefficient for both models. In addition to the reasons given in Singha and Gorelick (2006), other contributors of high scatter might be the use of a univariate correlation and moisture sampling in nonoptimal locations. From equations 15, 18, and 19, the saturation parameter is used to describe the bulk resistivity relationship, which incorporates saturated water content (or porosity), residual water content, and tortuosity. Furthermore, the bulk density is a spatially variable parameter. Therefore, Figure 5a might be a collapsed 1D view of a multivariate relationship.

The second issue of nonoptimal sampling stems from the basics of geophysics as a target recognition tool. For this problem, the targets are high and low resistivity regions that might be indicative of preferential flow into high-permeability and around low-permeability zones. Figures 4 and 5b and d show the location of characterization/stimulation wells into regions that mostly straddle the high and low resistivity. The wells were placed prior to the geophysics, with the result of an oversampling of the middle of the resistivity distribution. The lowest 3.5% of the resistivity values (below 36 ohm-m), for example, is not represented in the assay sampling, nor are values above 270 ohm-m found within the colocated data sets. Sampling the extremes could improve the relationship.

Figure 5b and d shows the conversion of resistivity to moisture for the linear fit and power fit, respectively. Figure 5c and e shows the equivalent of a cross validation, whereby the modeled moisture was compared to the measured moisture for colocated values. The con-

tours of modeled moisture within Figure 5b and d generally show the same shape of high and low moisture. For the linear fit, the underrepresentation of high resistivity values caused the conversion to calculate physically impossible negative moisture values. These were truncated to a value of zero. For the power fit, the underrepresentation of the low resistivity caused physically impossible moisture values above 1, and these values were truncated to 0.5. The scatter plots of Figure 5c and e focus on the physically reasonable moisture values between 0 and 0.3 g/g, accounting for 78% of the data.

The plots show the typical bias observed in other studies (Day-Lewis et al., 2005; Singha and Moysey, 2006), and Table 1 lists the statistics for the conversion. Both models overestimate the mean and variance of the moisture, and the residuals (modeled moisture-measured moisture) support the overestimation. The power model performs marginally better than the linear model, with a lower bias as demonstrated in the mean of the residuals.

Cokriging of moisture with resistivity

The spatial correlation of the moisture and resistivity data can be estimated with the covariance function. Figure 6a shows the experi-

Figure 5. (a) Scatter plot and models for colocated moisture and resistivity measurements, (b) moisture distribution from resistivity transformation using the linear model at an elevation of 1790 m, (c) validation of measured moisture versus modeled moisture for the linear model, (d) moisture distribution from resistivity transformation using the power model at an elevation of 1790 m, (e) validation of measured moisture versus modeled moisture for the power model. Coordinates are in Nevada State Plane, meters, North American datum of 1927.

mental covariance function and covariance model for the EC, and Figure 6b shows the cross-covariance information for the moisture and EC. The EC data were rescaled to the mean of the moisture data. The experimental covariance function for EC is smooth, and similar covariance models for geophysical data are shown by Parks and Bentley (1996). The spherical model was chosen to represent the covariance structure. The experimental cross-covariance function of Figure 6b also is generally less noisy than the moisture covariance function. There appears to be a reduction in $C^{zv}(0) - C^{zv}(h)$ at lags greater than 100 m, which likely is picking up on the sizable resistivity features that appear with a periodicity of about 100 m. At first glance, the cross-covariance model appears to be a poor fit to the shorter lags. The linear model of coregionalization forces the use of particular parameters for the model, as described in equation 9. Again, Parks and Bentley (1996) observe that the cross-covariance model is not the best visual fit to the experimental data.

Using the covariance and cross-covariance models of Figures 3 and 6, the data were cokriged with the program COKRI, using the ordinary cokriging option. The program is run with several parameters that control the number and distance of data to use in estimating the moisture at unsampled locations. Two crucial parameters are the formulation of the "**model**" and "**c**" matrices, which describes the covariance model and the parameters for the model. For this application, these matrices were set to

$$\mathbf{model} = \begin{bmatrix} \text{nugget} & 1 \\ \text{model}_1 & {}_1a^z \\ \text{model}_2 & {}_2a^z \end{bmatrix} = \begin{bmatrix} 1 & 1 \\ 4 & 40 \\ 4 & 100 \end{bmatrix} \tag{21}$$

and

$$\mathbf{c} = \begin{bmatrix} {}_0c^z & {}_0c^{zv} \\ {}_0c^{zv} & {}_0c^v \\ {}_1c^z & {}_1c^{zv} \\ {}_1c^{zv} & {}_1c^v \\ {}_2c^z & {}_2c^{zv} \\ {}_2c^{zv} & {}_2c^v \end{bmatrix} = \begin{bmatrix} 4.0 & 1.5 \\ 1.5 & 6.0 \\ 4.0 & 0.7 \\ 0.7 & 2.4 \\ 0.3 & 0.2 \\ 0.2 & 0.4 \end{bmatrix} \times 10^{-4}, \tag{22}$$

where the first column of "**model**" represents the model to use (1 = nugget, 4 = spherical), and the second column consists of the ranges. Marcotte (1991) describes in more detail how the matrices are formulated.

Figure 6c shows the results of cokriging for moisture over the heap. Again, the 1680 electrode positions were used to establish the locations of the unsampled moisture at an elevation of 1790 m. The results look markedly different from the original kriged version of Figure 3 away from the wells, and show some similarities to the results of Figure 5. The region near the cluster of wells in the east shows the highest moisture, even

though this was not the site of the lowest resistivity. The north-south banded nature of the resistivity in the western half of the survey area is retained also in the cokriging results but generally shows lower moisture. The region is undersampled relative to the east, likely contributing to the estimated moisture being lower.

The cross-validation test results in Figure 6d and e show how well the cokriging performed. For the point-based cross validation, the results are quite similar to those of the kriging. There appears to be sufficient support from the remaining moisture data within individu-

al boreholes to reconstruct the missing data point. The resistivity data add nothing for this interpolation. However, the real strength of the cokriging method is seen in Figure 6e, in which the well-based cross validation shows a much better performance than kriging and LSR. Where kriging produced a flatline response with almost no variability in unsampled data 40 m away from the measurement location, and LSR produced nonphysical estimations with very high variability, the cokriging method appears to be a hybrid of these two methods. Cokriging produces higher variability than kriging with physically meaningful moisture values. The statistics of Table 1 also show that the cokriging of moisture is closer to the mean and variance of the measured moisture than the other techniques with a much lower bias in the residuals. The rms, which tends to favor higher errors, also is the lowest for the cokriging method.

The cokriging method appears to work reasonably well considering the nonoptimal sampling. Even if the method cannot reproduce the measured moisture exactly, and there is uncertainty in the cross validation, the method can be used to find targets of potential dry spots missed during the primary leaching cycle. Figure 6c shows the location of recommended drilling spots based on the estimated driest areas of the pad. Once drilled and assayed, the moisture data can be reinterpolated to hone the spatial distribution. In this way, the geophysics and assaying can be conducted iteratively to extract more gold during the secondary leaching cycle.

CONCLUSIONS

A rock pile was characterized for the potential application of secondary recovery. The characterization methods included hard data from drilling and soft geophysical data from electrical resistivity. The samples from drilling were obtained every 1.5 m vertically from 29 well locations, but the wells were spaced too far apart to provide sufficient lateral resolution alone. The resistivity data were acquired along 12 parallel lines of approximately 400 m in length, and were subsequently inverse modeled in three dimensions. The cokriging method was used to supplement the measured moisture data with electrical resistivity to produce a map of potential dry spots within the pile.

The cokriging results demonstrated advantages over kriging the moisture data alone and least-squares regression (LSR) of the resistivity-versus-moisture scatter plot of colocated measurements. The correlation length of the moisture measurements was shorter than the average well spacing, making the kriged moisture appear rather homogeneous away from the sampling point. At approximately 40 m away from the well, the estimated moisture reverted to the average value of the sampled data. This gave the kriged moisture a bull's-eye appearance around the well. The
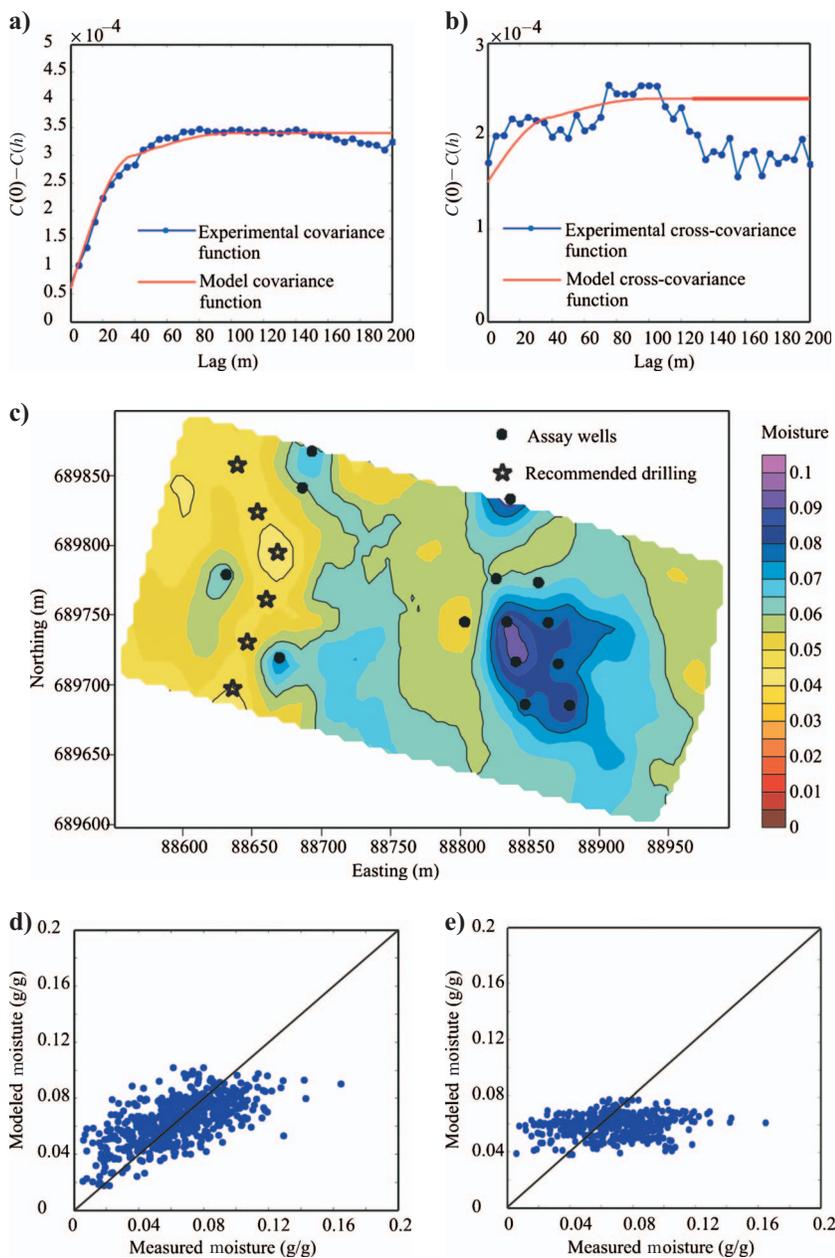
Figure 6. Cokriging of moisture data using 3D electrical resistivity, (a) experimental covariance function and covariance model for a scaled electrical resistivity (as conductivity), (b) cross-covariance modeling of moisture and scaled electrical conductivity, (c) moisture distribution from cokriging with moisture and conductivity at an elevation of 1790 m, (d) cross-validation results from a point-based removal procedure, (e) cross-validation results from a well-based removal procedure. Coordinates are in Nevada State Plane, meters, North American datum of 1927.

cokriging method provided a means for interwell interpolation. The moisture from the LSR method mimics the resistivity distribution because the method is conducted by simple transformation of the resistivity. For this example, the LSR moisture produced physically unrealistic values 20% of the time, and the ordinary cokriging method ensured that the estimated moisture falls within the bounds of the measured moisture. The cross-validation results also revealed that the cokriging method reproduced the mean and variance of the sampled data much better than kriging or LSR, while also having the lowest bias in the residuals. However, the general indirect relationship between resistivity and moisture would allow the LSR method to be a starting point for initial characterization of rock piles by guiding the drilling program.

It is recommended that the cokriging with resistivity and assay data be conducted iteratively by introducing the assay data as it becomes available. In this way, the moisture distribution can be updated to site new wells better. Even if the cokriging method cannot reproduce with exact fidelity the moisture distribution of the pile, it likely would locate the driest portions of the heap indicative of regions bypassed during primary leaching. It is anticipated that the savings in drilling through proper well siting would more than offset the cost of geophysics.

ACKNOWLEDGMENTS

REFERENCES

Advanced Geosciences, Inc., (AGI), 2008, Instruction manual for EarthImager 3D, Version 1.5.3 resistivity inversion software, http://www.agiusa.com/, accessed 3 November 2009.
Ahmed, S., and G. de Marsily, 1993, Cokriged estimation of aquifer transmissivity as an indirect solution of the inverse problem: A practical approach: Water Resources Research, **29**, 521–530.
Asch, T. H., M. Deszcz-Pan, B. L. Burton, and L. B. Ball, 2008, Geophysical characterization of American River levees, Sacramento, California, using electromagnetics, capacitively coupled resistivity, and dc resistivity: U. S. Geological Survey Open-File Report 2008-1109, http://pubs.usgs.gov/of/2008/1109/, accessed 9 November 2009.
Bhakta, P., and B. Arthur, 2002, Heap bio-oxidation and gold recovery at Newmont mining: First-year results: JOM: Journal of the Minerals, Metals and Materials Society, **54**, 31–33.
Bouffard, S. C., and D. G. Dixon, 2007, Evaluation of kinetic and diffusion phenomena in cyanide leaching of crushed and run-of-mine gold ores: Hydrometallurgy, **86**, 63–71.
Burkin, A. R., 2001, Chemical hydrometallurgy: Theory and principles: Imperial College Press.
Bussian, A. E., 1983, Electrical conductance in a porous medium: Geophysics, **48**, 1258–1268.
Campos, D., M. Chouteau, and M. Aubertin, 2003, Using geophysical methods to image the internal structure of mine waste rock piles: 9th European Meeting of Environmental and Engineering Geophysics, Paper O–008.
Crundwell, F., and S. A. Godorr, 1997, A mathematical model of the leaching of gold in cyanide solutions: Hydrometallurgy, **44**, 147–162.
Dannovski, G., and U. Yaramanci, 1999, Estimation of water content and porosity using combined radar and geoelectrical measurement.: European Journal of Environmental and Engineering Geophysics, **4**, 71–85.
Day-Lewis, F. D., K. Singha, and A. Binley, 2005, The application of petrophysical models to radar and electrical resistivity tomograms: Resolution dependent limitations: Journal of Geophysical Research, **110**, B08206.
De Andrade Lema, L. R. P., and D. Hodouin, 2005, A lumped kinetic model for gold ore cyanidation: Hydrometallurgy, **79**, 121–137.
Descloitres, M., O. Ribolzi, Y. L. Troquer, and J. P. Thiébaux, 2008, Study of water tension differences in heterogeneous sandy soils using surface ERT:

Journal of Applied Geophysics, **64**, 83–98.
Deutsch, C. V., and A. G. Journel, 1992, GSLIB: Geostatistical software library and user's guide: Oxford University Press.
Dey, A., and H. F. Morrison, 1979, Resistivity modeling for arbitrarily shaped three-dimensional structures: Geophysics, **44**, 753–780.
Dong, P., J. Fan, Z. Chen, L. Wang, X. Gao, and R. Qin, 2008, Applying mise-a-la-masse method to determine the length of reinforcement in bored in situ concrete piles: Journal of Environmental and Engineering Geophysics, **13**, 51–56.
Edwards, R. N., 1997, On the resource evaluation of marine gas hydrate deposits using sea-floor transient electric dipole-dipole methods: Geophysics, **62**, 63–74.
Garambois, S., P. Sénéchal, and H. Perroud, 2002, On the use of combined geophysical methods to assess water content and water conductivity of near-surface formations: Journal of Hydrology, **259**, 32–48.
Gloaguen, E., D. Marcotte, B. Giroux, C. Dubreuil-Boisclair, M. Chouteau, and M. Aubertin, 2007, Stochastic borehole radar velocity and attenuation tomographies using cokriging and cosimulation: Journal of Applied Geophysics, **62**, 141–157.
Grellier, S., R. Guérin, H. Robain, A. Bobachev, F. Vermeersch, and A. Tabbagh, 2008, Monitoring of leachate recirculation in a bioreactor landfill by 2-D electrical resistivity imaging: Journal of Environmental and Engineering Geophysics, **13**, 351–359.
Gunther, T., C. Rucker, and K. Spitzer, 2006, Three-dimensional modeling and inversion of dc resistivity data incorporating topography: 2 — Inversion: Geophysics Journal International, **166**, 506–517.
Guzman, A. G., R. Scheffel, and S. Flaherty, 2008, The fundamentals of physical characterization of ore for leach, *in* C. A. Young, P. R. Taylor, and C. G. Anderson, eds., Hydrometallurgy 2008: Proceedings of the 6th International Symposium, 937–954.
Habashi, F., 1966, The theory of cyanidation: Transactions of Society for Mining, Metallurgy, and Exploration, **235**, 236–239.
Han, K. N., 2002, Fundamentals of aqueous metallurgy: Society for Mining, Metallurgy, and Exploration.
Iglesias, N., and F. Carranza, 1994, Refractory gold-bearing ores: A review of treatment methods and recent and advances in biotechnological techniques: Hydrometallurgy, **34**, 383–395.
Isaaks, E. H., and R. M. Srivastava, 1989, An introduction to applied geostatistics: Oxford University Press.
Juvonen, R., and E. Kontas, 1999, Comparison of three analytical methods in the determination of gold in six Finnish gold ores, including a study on sample preparation and sampling: Journal of Geochemical Exploration, **65**, 219–229.
Keller, G. V., 1988, Rock and mineral properties, *in* M. N. Nabighian, ed., Electromagnetic methods in applied geophysics, v. 1: SEG, 13–51.
Kennedy, B. A., 1990, Surface mining: Society for Mining, Metallurgy, and Exploration.
Kunkel, J. R., and J. Arnold, 2008, Flow through leach pads — Perception versus reality, *in* C. A. Young, P. R. Taylor, and C. G. Anderson, eds., Hydrometallurgy 2008: Proceedings of the 6th International Symposium, 906–911.
LaBrecque, D. J., M. Miletto, W. Daily, A. Ramirez, and E. Owen, 1996, The effects of noise on Occam's inversion of resistivity tomography data: Geophysics, **61**, 538–548.
Li, Y., and D. W. Oldenburg, 1994, Inversion of 3-D DC resistivity data using an approximate inverse mapping: Geophysical Journal International, **116**, 527–537.
Loke, M. H., and R. D. Barker, 1996, Practical techniques for 3D resistivity surveys and data inversion: Geophysical Prospecting, **44**, 499–523.
Marcotte, D., 1991, Cokriging with Matlab: Computer and Geosciences, **17**, 1265–1280.
——, 1993, Corrigendum: Computer and Geosciences, **19**, 871.
Marsden, J., and I. House, 1992, The chemistry of gold extraction: Ellis Horwood.
Mills, B. A., 1985, Geology of the Round Mountain gold deposit: Nye County, Nevada, *in* V. F. Hollister, ed., Discoveries of epithermal precious metal deposits: Case histories of mineral discoveries, v. 1: Society of Mining Engineers of The American Institute of Mining, Metallurgical, and Petroleum Engineers, 104–114.
Osazuwa, I. B., and A. D. Chinedu, 2008, Seismic refraction tomography imaging of high-permeability zones beneath an earthen dam, in Zaria area, Nigeria: Journal of Applied Geophysics, **66**, 44–58.
Parks, K. P., and L. R. Bentley, 1996, Enhancing data worth of EM survey in site assessment by cokriging: Ground Water, **34**, 597–604.
Poisson, J., M. Chouteau, M. Aubertin, and D. Campos, 2009, Geophysical experiments to image the shallow internal structure and the moisture distribution of a mine waste rock pile: Journal of Applied Geophysics, **67**, 179–192.
Rucker, D. F., A. Schindler, M. T. Levitt, and D. R. Glaser, 2009a. Three-dimensional electrical resistivity imaging of a gold heap: Hydrometallurgy, **98**, 267–275.
Rucker, D. F., M. McNeill, A. Schindler, and G. E. Noonan, 2009b, Monitor-

ing of a secondary recovery application of leachate injection into a heap: Hydrometallurgy, **99**, 238–248.

Seal, T., 2004, Enhanced gold extraction in cyanide heap leaching using Hydro-Jex technology: Ph.D. dissertation, University of Idaho.

——, 2007, Hydro-Jex: Heap leach pad stimulation technology; ready for world wide industrial adoption?: 2007 Annual Meeting, Society of Mining Engineers, Proceedings, Paper 07-123.

Sen, P. N., 1997, Resistivity of partially saturated carbonate rocks with microporosity: Geophysics, **62**, 415–425.

Singha, K., F. D. Day-Lewis, and S. Moysey, 2007, Accounting for tomographic resolution in estimating hydrologic properties from geophysical data, *in* D. W. Hyndman, F. D. Day-Lewis, and K. Singha, eds., Subsurface hydrology: Data integration for properties and processes: American Geophysical Union Geophysical Monographs, 171, 227–242.

Singha, K., and S. M. Gorelick, 2006, Effects of spatially variable resolution on field-scale estimates of tracer concentration from electrical inversions using Archie's law: Geophysics, **71**, no. 3, G83–G91.

Singha, K., and S. Moysey, 2006, Accounting for spatially variable resolution in electrical resistivity tomography through field-scale rock physics relations: Geophysics, **71**, no 4, A25–A28.

Taylor, S., and R. Barker, 2006, Resistivity of partially saturated Triassic sandstone: Geophysical Prospecting, **50**, 603–613.

Topp, G. C., and P. A. Ferré, 2002, The soil solution phase, *in* J. H. Dane, and G. C. Topp, eds., Methods of soil analysis: Part 4 — Physical methods: Soil Science Society of America.

Waxman, M. H., and L. J. M. Smits, 1968, Electrical conduction in oil-bearing sands: Society of Petroleum Engineers Journal, **8**, 107–122.